ARTICLE

Atomic Layer Deposition of Photoelectrocatalytic Material on 3D-Printed Nanocarbon Structures†

Received 00th January 20xx,
Accepted 00th January 20xx

DOI: 10.1039/x0xx00000x

Siowwoon Ng, [a] Raul Zazpe,[b,c] Jhonatan Rodriguez-Pereira,[b,c] Jan Michalička,[c] Jan M. Macak,[b,c] and Martin Pumera*[,a]

3D-printing is an excellent tool for the prototyping and fabrication of a variety of devices. The ability to rapidly create on demand structures opens the vast possibilities for the innovations in catalysis and energy conversion/storage devices. The major bottleneck is that the materials which are suitable for 3D-printing usually do not possess the required energy conversion/storage ability. Atomic layer deposition (ALD) strategically offers homogeneous and conformal deposition of functional layers without compromising the 3D topography. Here, we show that readily fabricated fused deposition modeling extruded nanocarbon/polylactic acid (PLA) electrodes can be modified by a photoelectrocatalytic material with atomic precision. We use an archetypal material, MoS_2, with high electrocatalytic hydrogen evolution reaction (HER) activity, whilst possesses high photons absorption in the visible spectral region. We optimized the ALD process at low temperature to coat 3D-printed nanocarbon/PLA electrodes with different number of MoS_2 ALD cycles for photoelectrocatalytic HER. We present for the first time, the feasibility of low temperature transition metal dichalcogenide coatings on 3D-printed nanocarbon surface, unequivocally elevate the benchmark of functional coatings by ALD on any 3D-printed platforms.

Introduction

Additive manufacturing or its general term three-dimensional (3D)-printing was initially developed for instant prototyping of objects in realistic aesthetics. Presently, it is one of the major innovative solutions in producing complex 3D structures.[1] Its diverse practicality has triggered an accelerated advancement in electronics, aircraft, automotive, orthopedic implant, gas, and oil industries.[2] 3D-printing is increasingly popularized through its fascinating features to create a vast variety of materials, such as polymers, ceramics, and metals, where any shapes, designs, and dimensions with delicate details can be created locally and instantaneously.[2–4]

3D-printing has gradually expanded to electrochemical energy conversion and storage (EECS) applications, with a wide array of 3D designs tested as EECS devices. A few intricate 3D structures are interdigitated finger electrode for (micro-)supercapacitors,[5–7] high-aspect-ratio interdigitated architectures and highly flexible twisted-fibers for micro-batteries,[8,9] helical- and gauze-shaped electrodes for water-splitting electrocatalysts.[10,11] These electrodes were fabricated by different 3D-printing techniques to fulfill the material or the required properties. Selective laser melting (SLM) technique utilizes a high-powered laser beam to melt and fuse the metal powder particles to construct the desired 3D metal electrodes.[10,11] Meanwhile, inkjet printing (IJP) and direct ink writing (DIW) techniques offer more diverse range of materials to create functional 3D electrodes. For smooth printing performance, the key success is the critical optimization of the rheological properties of the "ink" that is comprised of one or more active materials, additives, and suitable solvent.[1,4] In parallel, fused deposition modeling (FDM) technique utilizing composite filaments consist of thermoplastic and carbon-based material has emerged as a captivating option because of its ease of printing. FDM printing can be realized by a benchtop 3D printer for complicated and detailed structures designed by computer aided software,[12] and further simplified by a hand-held 3D-printing pen for ultrafast printing of simple structures.[13] Following the printing of electrodes, the insulating thermoplastic which acts as the printing support is adequately removed to achieve conductive 3D nanocarbon electrodes.[14–16] The optimized 3D nanocarbon electrodes offer two major advantages, i) simpler design or planar structure that is ready to be used as independent electrodes similar to that of conventional glassy carbon or screen-printed carbon electrodes in electroanalytical studies,[16,17] and ii) customized design as a supporting platform to accommodate functional materials. The latter has been practically demonstrated by a variety of materials such as conductive polymers,[18,19] metals,[18,20]

[a] Future Energy and Innovation Laboratory, Central European Institute of Technology, Brno University of Technology, Purkyňova 123, 61200 Brno, Czech Republic.
Email: pumera.research@gmail.com
[b] Center of Materials and Nanotechnologies, Faculty of Chemical Technology, University of Pardubice, Nam. Cs. Legii 565, 53002 Pardubice, Czech Republic.
[c] Central European Institute of Technology, Brno University of Technology, Purkyňova 123, 61200 Brno, Czech Republic.

†Electronic Supplementary Information (ESI) available: Additional XPS spectra, XRD pattern, Raman spectrum, SEM-EDX elemental maps, EIS Nyquist plots, Table for comparison of MoS_2 supported by 3D-printed electrodes, HER Tafel plots, Table for Tafel slopes, and chronoamperometry stability test. See DOI: 10.1039/x0xx00000x

MXene,[21] and transition metal dichalcogenides (TMDs)[7,22–25] in EECS areas including electrocatalysts, supercapacitors, and batteries.

In the quest for efficient catalysts for clean energy conversion, earth-abundant materials are in continuous pursuit as alternatives to the highly-scarce platinum catalyst. Apart from the noble metals, the core members of TMDs such as MoS_2, WS_2, $MoSe_2$, WSe_2, have demonstrated the highest catalytic activities across metals, oxides, and chalcogenides.[26,27] Of particular relevance, MoS_2 is identified as the most actively investigated catalyst among TMDs because of its near metallic conductivity, high carrier mobility, and most critically, relatively good photo-corrosion stability.[28,29] For catalytic activities, the exposed edges of MoS_2 are active sites for hydrogen evolution and photocatalytic reactions.[30,31] Computational and experimental findings have shown that MoS_2 possesses favorable Gibbs free energy (ΔG_H) for hydrogen adsorption. Moreover, its optical band gap between 1.2-1.9 eV and high absorptivity spanning across the visible spectral region conveniently harvest plenteous solar energy.[32–34]

For these peculiar properties, MoS_2 has been synthesized through exfoliation, hydrothermal, electrodeposition, reactive magnetron sputtering, chemical vapor deposition (CVD), and atomic layer deposition (ALD).[24,35–40] ALD is an advanced deposition technique and its signature feature is to produce conformal deposition according to the topography of the targeted object. This deposition technique is particularly suitable for complex structures with obscured areas, such as 3D-printed objects. As a derivative of the CVD process, ALD primarily takes place at an elevated temperature. In some cases, the precursors are necessarily heated up to increase the vapor pressure for sufficient precursor dosing, and the deposition chamber is maintained at a certain temperature to prevent precursor condensation.[41] In general, low reaction temperatures are unable to produce sufficient thermal energy to drive the reactions between surface groups and reactants. Hence, higher precursor dose or longer exposure time is introduced to compensate for the chemical reactions.[42] Nevertheless, for ALD MoS_2, despite different combinations of Mo and S precursors have been experimented, low temperature ALD remains highly challenging due to the incompatibility between the two precursors to ensure high reactivity and volatility for a self-limiting surface reaction.[36,43] These stringent conditions become a major hindrance for substrates with low thermal deformation temperature, for instance, polymer, plastic, cellulose, and nanocarbon/PLA based electrodes.

In view of the low operating temperature of the FDM-produced nanocarbon electrodes, previously, we employed electrodeposition at room temperature and obtained amorphous MoS_2 structure for solid-state supercapacitor.[7] The option of post-thermal treatment at 500-1000 °C to improve the crystallinity of MoS_2 is not feasible for these electrodes.[36,44] Separately, ALD was performed at low substrate temperature that resulted in amorphous Al_2O_3 for electrochemical oxidation of 1,2-dihydroxybenzene to *o*-benzoquinone.[45] To sustain the high substrate temperature for ALD, stainless steel electrodes were used for the deposition of anatase TiO_2 for photoelectrochemical water oxidation.[46]

In this work, we challenge the ALD limits at low temperature to deposit a quintessential TMDs member, i.e. MoS_2 nanoclusters on customizable 3D-printed nanocarbon electrodes while preserving the structural integrity of the electrodes, for photoelectrocatalytic hydrogen evolution reaction (HER) as illustrated in the Scheme 1. The present work advances the ALD technique on 3D-printed platforms, where the depositions are no longer constrained to conventional metal oxides or on 3D metallic objects.[45,46] Following this work, low temperature ALD of other interesting chalcogenides on any creative 3D platforms can be achieved for applications beyond photo- and electrochemistry.

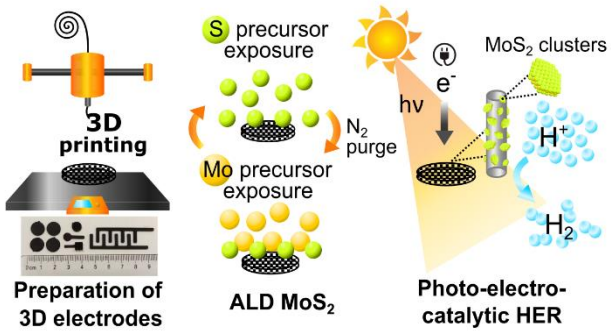

Scheme 1 Schematic illustration of the preparation of 3D-printed nanocarbon/polylactic acid electrode by fused deposition modelling technique, followed by atomic layer deposition (ALD) of a functional coating, MoS_2 nanoclusters on the 3D-printed nanocarbon electrode for photoelectrocatalytic hydrogen evolution reaction (HER).

Experimental

Preparation of 3D-printed nanocarbon electrodes

The electrodes were prepared according to our previously optimized procedures.[14] Briefly, a partial infill 3D electrodes were designed and printed by a 3D printer (Prusa i3 MK3 printer, Prusa research, Czech Republic) fed with commercial BlackMagic3D graphene/PLA composites filament. To activate the electrodes, the carbonization process was carried out in a furnace with heating rate 5 °C min^{-1} up to 350 °C for 3 h in air ambient, followed by natural cooling to room temperature.

Atomic layer deposition of MoS_2

The deposition of MoS_2 was carried out via atomic layer deposition (ALD, Beneq TFS-200). Bis(t-butylimido)bis(dimethylamino)molybdenum(VI) (Strem, 98%) and H_2S (Messer, 99.5%) were used as Mo and S precursors, respectively. The Mo precursor was heated up to 75 °C to increase its vapor pressure. The deposition conditions were 190 °C, base pressure 2 mbar, using N_2 (99.9999%) as carrier gas at a flow rate of 500 standard cubic centimeters per minute (sccm) in a continuous flow process. Under these conditions, one ALD growth cycle was defined by the following sequence: H_2S pulse (1.25 s) – N_2 purge (15 s) – Bis(tbutylimido)bis(dimethylamino)molybdenum(VI) pulse (2 s)

- N_2 purge (15 s). The number of MoS_2 ALD cycles, N_{ALD}, deposited onto the 3D-printed nanocarbon electrodes were: 38, 75, 150, 300, 600, and 900.

Materials characterizations

The surface chemical composition analysis of the blank and ALD MoS_2 3D-printed nanocarbon electrodes was performed by X-ray photoelectron spectroscopy (XPS, ESCA2SR, Scienta-Omicron) using monochromatic Al Kα (1486.7 eV) excitation source. The quantitative analysis was carried out by using the elemental sensitivity factors provided by the manufacturer. Structural analysis was carried out by X-ray diffraction (XRD) using a diffractometer (SmartLab 3kW, Rigaku) with Bragg-Brentano geometry. A Cu lamp was operated at a current of 30 mA and a voltage of 40 kV with Cu Kα radiation (λ = 1.54 Å) equipped by 1D-detector Dtex-Ultra. Raman measurement was conducted by Raman spectroscopy (Alpha 300R, WITec) using a laser excitation source (λ = 532 nm) with a power of 25 mW. The surface morphology was examined by scanning electron microscope (SEM, Verios 460L, Thermo Fisher Scientific). Elemental analysis was carried out by energy-dispersive X-ray (EDX) with SDD Octane Super spectrometer (EDAX) integrated with the SEM used for imaging with an accelerating voltage of 18 kV. The high-resolution (scanning) transmission electron microscope (HR-TEM, STEM) imaging and both STEM-EDX and STEM-electron energy loss spectroscopy (EELS) analysis were obtained by spherical aberration image (C_s)-corrected TEM (TITAN Themis 60-300, Thermo Fisher Scientific) operated at 300 keV. The STEM-EDX analysis was performed with SUPER-X spectrometer with four 30 mm^2 windowless detectors. The EDX data were processed in Velox software v2.12 (Thermo Fisher Scientific). The STEM-EELS analysis was performed with a GIF Quantum ERS/966 post-column energy filter (Gatan) at acceleration voltage of 300 kV and with the use of beam current 100 pA, pixel time of 0.1 s, pixel size of 3 Å, convergence semi-angle of 10 mrad, collection semi-angle of 28.2 mrad, camera length of 29.5 mm and entrance aperture of 2.5 mm. The EELS data were processed in GMS3 software v3.41 (Gatan).

Photo- and electrocatalytic activities measurements

All voltammetric, chronoamperometric, and impedance experiments were performed by a potentiostat (PGSTAT 204, Metrohm Autolab) connected to a computer operated by NOVA software v2.1. The three-electrode configuration consists of blank or ALD MoS_2 coated 3D-printed nanocarbon electrodes, platinum wire and Ag/AgCl (1 M KCl) as working, counter and reference electrode, respectively. For the photocurrent response, chronoamperometry measurements were carried out in 10 mM $K_3[Fe(CN)_6]$ with 0.1 M KCl electrolyte. Light-emitting diodes (LEDs LZ4-40B208, LZ4-40G108, LZ4-40R208, LedEngin Inc.) with emission wavelengths, λ = 460 nm (≈55 mW/cm^2), 523 nm (≈100 mW/cm^2), and 660 nm (≈40 mW/cm^2), respectively, were served as the irradiation sources. The photocurrents were recorded by switching the light on/off at constant intervals, varying the applied potential with reference to Ag/AgCl in the range of 0.4 – 1.0 $V_{Ag/AgCl}$. For photo-assisted hydrogen evolution reaction (HER), linear sweep voltammetry (LSV) was performed with scan rate of 2 mV s^{-1} in 0.5 M H_2SO_4 electrolyte, with and without irradiation. The potential with reference to Ag/AgCl ($V_{Ag/AgCl}$) was converted to the potential with reference to reversible hydrogen electrode (V_{RHE}) according to the calculation in the literature.[47] Electrochemical impedance spectroscopy (EIS) measurement was carried out at open-circuit potential (OCP) in the frequency range from 10 kHz to 50 mHz in 10 mM $[Fe(CN)_6]^{3-/4-}$ with 0.1 M KCl electrolyte. Stability test was carried out by chronoamperometry measurement with ≈ -0.45 V_{RHE} in 0.5 M H_2SO_4 electrolyte for 8 h.

Results and discussion

The as-printed 3D nanocarbon/polylactic (PLA) electrodes (from commercially available 'graphene/PLA' composites filament from BlackMagic) were thermally treated at 350 °C to carbonize the excess PLA for improved electrical conductivity.[14] In a previous study, thermogravimetric analysis (TGA) carried out on the 3D electrodes printed by the same composite filament has revealed an ≈80 % removal of PLA at this annealing temperature.[15] Subsequently, we coated the nanocarbon electrode by MoS_2 via ALD process, with a wide range of ALD cycles, N_{ALD} = 38, 75, 150, 300, 600, and 900. The deposition was carried out at a substrate temperature of 190 °C by using bis(t-butylimido)bis(dimethylamino)molybdenum and H_2S as Mo and S precursors, respectively. To confirm that the ALD MoS_2 process was successful, we first investigate the surface chemical composition by X-ray photoelectron spectroscopy (XPS). Fig. 1A shows the XPS survey spectrum of the blank and 300 ALD cycles MoS_2 coated 3D-printed nanocarbon electrodes. All spectra recorded C, O, and Ti peaks from the carbon electrode (Ti is a common impurity in the PLA filament), and the addition of Mo, and S from MoS_2 coated electrode. Setting aside the most prominent C, the quantitative analyses of the survey spectrum present considerable atomic concentration of O and Ti. Other studies have validated the presence of Ti-based and Fe-based impurities in the commercial filament used in this work.[15,48] The Ti metal was partially transformed into TiO_2 during the thermal activation of the as-printed nanocarbon electrode.[15,48] To confirm the findings from the previous reports, high resolution scan for C 1s, Ti 2p, and O 1s spectra of the 300 ALD cycles are included in Fig. S1 of the ESI. The C 1s shows an intense peak centered at binding energy 284.0 eV, with a low shoulder composed of organic functional groups from the electrode. The Ti 2p spectrum exhibits spin-orbit split doublets Ti $2p_{3/2}$ and Ti $2p_{1/2}$ at 458.5 and 464.1 eV, respectively, which are the signature of Ti^{4+}-O. The O 1s spectrum presents an intense peak at 529.6 eV corresponding to metal oxides for Ti^{4+}-O and possibly $Mo^{4+/6+}$-O due to the partial surface oxidation or formation of Mo-O during the initial nucleation of the ALD process (details of the formation to be discussed later). Meanwhile, the broader shoulder of O 1s stretching over the higher binding energies suggests the presence of –OH and other organic groups. All in all, the O 1s peak can be tied to the major contribution of TiO_2, small amount from MoO_x, and the organic groups such as C-O and C=O from the nanocarbon electrode.

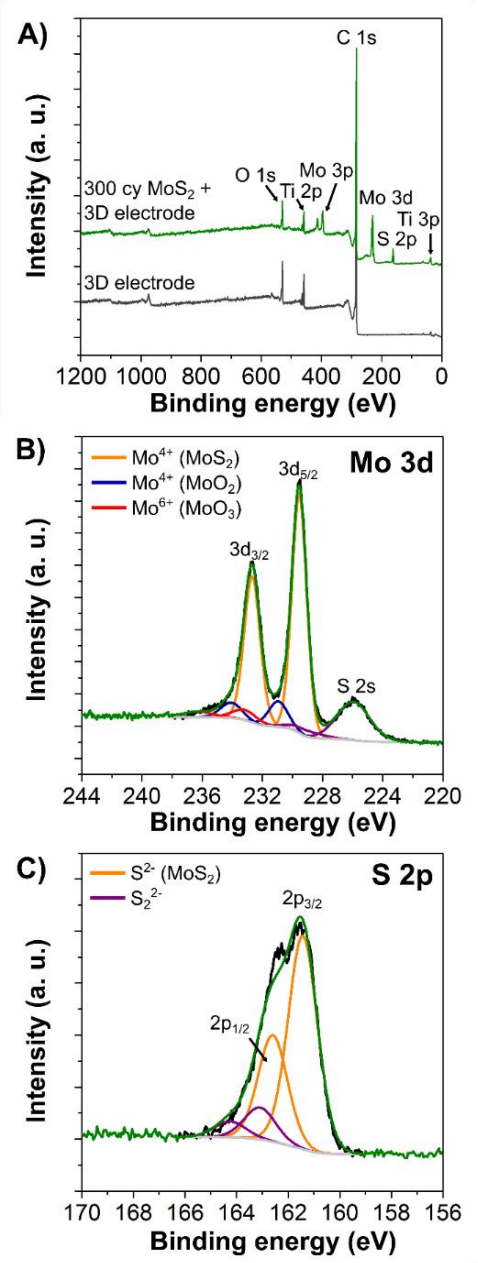

Fig. 1 (A) XPS survey spectra of blank and 300 ALD cycles MoS_2 coated 3D-printed nanocarbon electrodes. High-resolution core level spectra of (B) Mo 3d and (C) S 2p of 300 ALD cycles MoS_2 coated 3D nanocarbon electrodes.

With the MoS_2 coatings on the 3D-printed nanocarbon electrodes, the C and O signals from the carbon are slightly decreased in the survey spectra. We further analyze the high-resolution Mo 3d and S 2p spectra in Fig. 1B,C to evaluate the coated MoS_2. The Mo 3d spectrum presents intense spin-orbit split doublets for Mo $3d_{5/2}$ and Mo $3d_{3/2}$ at 229.5 and 232.7 eV, respectively, which are identified as the Mo^{4+} oxidation state for MoS_2. Additionally, the 225.9 eV peak at the lower energy position is assigned to S 2s, associated with the formation of MoS_2.[49] Two pairs of small doublets embedded at the higher energy regions are Mo^{4+} (231.0 and 234.1 eV) and Mo^{6+} (233.2 and 236.3 eV), which are responsible for MoO_2 and MoO_3,[50] respectively, complementing the observation from the O 1s spectra. Meanwhile, the S 2p spectrum shows the corresponding split doublets with S $2p_{3/2}$ and S $2p_{1/2}$ at 161.4 and 162.6 eV, respectively, as the S^{2-} oxidation state for MoS_2.[49] The small doublet is suggested to be the bridging disulfides, S_2^2, in agreement with the small S 2s at 229.1 eV in the Mo 3d region.[51,52] Altogether, these findings evident the formation of MoS_2, and the ratio of S/Mo calculated according to the Mo 3d and S 2p individual spectral areas in Fig. 1B,C results in ≈1.6, as a sulfur-deficient MoS_2. Across the literature, it is frequently noticed that the synthesized MoS_2 is not always stoichiometry and the ratio of chalcogen-to-metal varies from 1 to 3.[24,37–39,53,54] Interestingly, room temperature synthesis techniques generally produced chalcogen-rich TMDs whereas vapor depositions at elevated temperatures commonly yielded chalcogen-deficient TMDs. Perfectly stoichiometric TMDs grown via ALD require stringent conditions due to intricate factors including the surface chemistry of the substrate and the kinetics of the precursors. For instance, several as-grown ALD MoS_2 and $MoSe_2$ structures were reported to be non-stoichiometric,[39,53,55–57] and classical post-annealing at elevated temperatures was adapted to improve the stoichiometry and crystallinity.[36,39,44,57,58] However, the high annealing temperatures are incompatible in this work due to the potential disintegration of the 3D nanocarbon electrodes. We associate the overall sulfur-deficient behavior to the reasonably low growth temperature at 190 °C, which is also in agreement with other works.[39,57] To further investigate the 300 ALD cycles MoS_2 coated 3D-printed nanocarbon electrode, X-ray diffractometer and Raman spectroscopy measurements were carried out. Both X-ray diffraction (XRD) pattern and Raman spectrum in Fig. S2 of the ESI† recorded only the carbon and TiO_2 related peaks from the electrode.

Fig. 2A,B illustrate the scanning electron microscope (SEM) images of the blank and 300 ALD cycles MoS_2 coated nanocarbon electrodes. The activated 3D nanocarbon electrode consists of the structures of a fiber-like morphology with several micrometers in length.[59] The agglomerations of small particles are the evidence of remaining PLA remnants from the activation step. The 300 ALD cycles MoS_2 coated nanofibers show a slightly different textural surface as compared to the uncoated nanofibers. Considering the difficulties to visualize the coated MoS_2, especially when the deposition closely follows the complex morphology of the nanofibers, subsequent analyses were performed by a high-resolution-transmission electron microscope (HR-TEM). The HR-TEM image in Fig. 2C reveals that nanofibers are hollow, effectively representing the crystallized multi-wall carbon tubes. The scanning TEM (STEM) with high-angle annular dark field (HAADF) image in Fig. 2D clearly distinguishes the cluster-like MoS_2, which is supported by the STEM-energy dispersive X-ray (EDX) analysis via elemental mapping of Mo and S, shown in Fig. 2E,F. As the X-ray energies of Mo-L shell and S-K shell are very close to each other, it is rather impossible to differentiate between the two elements. Nevertheless, the EDX maps serve as a reference to indicate the uniform distribution of both elements on the carbon surface. In addition, homogeneous coverage of Mo and S on a larger scale surface was confirmed by the large area SEM-EDX elemental

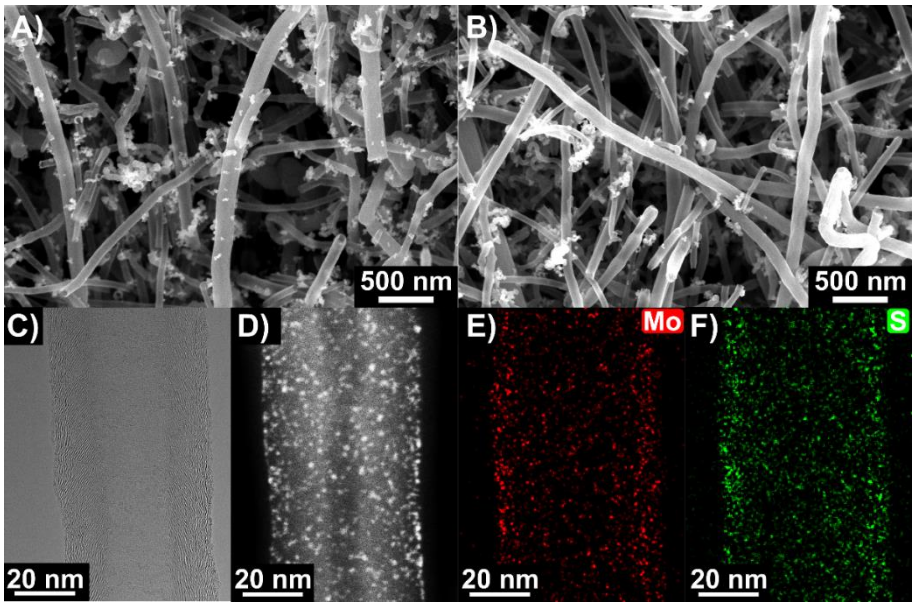

Fig. 2 SEM images of (A) blank and (B) 300 ALD cycles MoS_2 coated 3D-printed nanocarbon electrodes. A single tube extracted from 300 ALD cycles MoS_2 coated electrode for (C) HR-TEM and (D) STEM-HAADF imaging, and the corresponding STEM-EDX chemical elemental maps for (E) molybdenum and (F) sulfur show the uniform distribution of both elements along the carbon tube. The signal in STEM-EDX maps was presented in intensities with retracted background, deconvoluted peaks, and pre-filtered signals via pixel averaging for higher precision.

mapping of the MoS_2 coated 3D-printed nanocarbon electrode. Besides, C, O, Ti, and Fe originated from the 3D printing nanocarbon/PLA filament were also detected. The presence of Ti and Fe are related to the impurities as discussed in the XPS section. The mapped area and individual elemental maps are included in Fig. S3 of the ESI.

A closer inspection on the edge of the carbon tube wall in Fig. 2C is presented as a detailed HR-TEM image in Fig. 3A. Interestingly, the deposits are identified in the form of atomic clusters at the carbon surface. An example of a cluster is analyzed from the area of interest marked by a red rectangle in Fig. 3A and further enlarged in Fig. 3B,C as the raw image and mathematically filtered image via inversed fast Fourier transformation (IFFT), respectively. The atomic cluster is discernible in a honeycomb-like arrangement, which is typical for MoS_2. The IFFT pattern in Fig. 3D derived from Fig. 3B reveals the bright spots laying at a radius of 2.67 Å that matches the {101} lattice planes with the *d*-spacing of 2H-MoS_2 with hexagonal crystal structure, space group P63/mmc.[60] Considering that the spot positions are divided by ≈60°, the observed crystal is oriented close to the zonal axis ***z*** = [001]. Noticeably, the crystalline structure is resolved here but it is not being observed in the XRD pattern. This is resonated with the nanoscaled MoS_2 clusters, even by the accumulation of smaller clusters to form larger clusters, the MoS_2 possesses a significantly smaller volume than the bulk nanocarbon electrode as shown by Fig. 3A.

Given the limitation of STEM-EDX spectroscopy for elemental analysis, STEM-electron energy loss spectroscopy (EELS) was additionally employed to perform elemental mapping of a larger MoS_2 cluster at the edge of another carbon tube, marked by a red rectangle in Fig. 3F. The maps of Mo, S, C, and the overlay of all three elements are compiled as Fig. 3G-J. The EELS spectrum in Fig. 3K acquired from the marked area on the HAADF image in Fig. 3F presents the apparent edges of S–L and Mo–M, which strongly evidences that the cluster consists of Mo and S, and the C-K edge from the carbon tube wall.

The results from different investigation techniques concertedly demonstrate that the ALD of MoS_2 on 3D-printed nanocarbon electrode produces MoS_2 atomic clusters which stochastically coalesce into nanocluster with flaky feature on the surface of carbon tube. The flaky feature of MoS_2 depicted in Figs. 2D and 3E is commonly observed for TMDs grown by ALD technique, such as MoS_2,[29,53] WS_2,[61] and $MoSe_2$[56] flakes are vertically oriented on the surface of the substrate, instead of forming smooth and continuous films. The nano-scaled clusters[31,62] and flakes[53,61] morphology of TMDs with more exposed catalytic sites are reportedly energetically favorable for hydrogen evolution. In fact, the growth morphology is typically influenced by the initial nucleation to induce the subsequent lateral or vertical grain growth. To initiate an ALD process, the presence of O-H groups on the surface as active sites is essential for the adsorption of the reactive precursor. As the carbon-based surface is rather chemically inert, the nucleation occurs mainly at the defect sites.[63] We designed the ALD process that for the first half cycle, H_2S pulse was first introduced to create additional S-H groups, on top of the limited O-H groups. When Mo precursor was introduced in the second half cycle, both S-H and O-H functional groups react with Mo to form S-Mo and O-Mo at the interface between carbon and MoS_2. The succeeding ALD pulses then lead to the subsequent growth of MoS_2. This corroborates the coexistence of MoS_2 and a small amount of MoO_x in the Mo 3d XPS spectrum in Fig. 1B. Overall, we

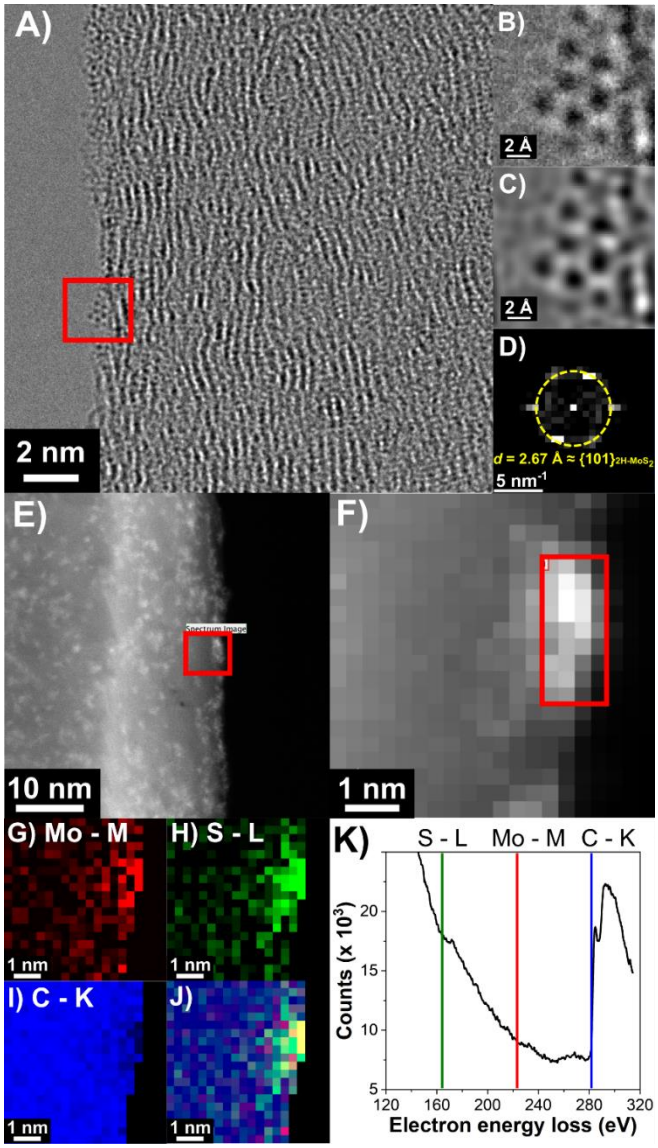

Fig. 3 HR-TEM-related analyses on a 300 ALD cycles MoS_2 coated carbon tube. (A) Detailed HR-TEM image at the edge of carbon tube shows that the coated MoS_2 is in the form of atomic clusters. (B) Raw image and (C) mathematically filtered image via IFFT, taken from the area marked by the red rectangle in (A) reveals that the atomic cluster is arranged in a honeycomb-like crystalline structure, typical for MoS_2. (D) FFT pattern obtained from (B) confirms the crystalline structure of MoS_2. (E, F) STEM-HAADF images of a larger MoS_2 cluster for STEM-EELS elemental mapping (G-I) molybdenum, sulfur, and carbon, and (J) overlay of all elements. Each pixel in the colored images (G-J) represents the intensities of the detected signal of each specific element, after background subtraction and quantification. (K) EELS spectrum with apparent edges of S-L and Mo-M from a MoS_2 cluster along with the C-K edge from the carbon tube, the spectrum was acquired from the area marked by the red rectangle in (F).

transformed the disadvantage of carbon surface to advantage, where the growth of discontinuous MoS_2 film resulted in the island-growth of nanoclusters with increased active edge proportions.

Having ascertained that MoS_2 nanoclusters were synthesized, we investigate the feasibility of the MoS_2 coated 3D nanocarbon electrodes as photoelectrocatalysts. To begin, we evaluate the photo-response of all 38 to 900 ALD cycles MoS_2 coated electrode by irradiating a light source of 660 nm wavelength with a constant potential of 1.23 V_{RHE}. The photo-response is monitored by the change in photocurrent densities recorded in Fig. 4A with periodical alternation between the on and off state of the light source. An overall increasing trend of photocurrent densities from ≈0.2 mA cm^{-2} to a maximum of ≈0.6 mA cm^{-2} was observed with the gradual addition from 38 to 600 ALD cycles. Between 600 and 900 ALD cycles, the increase in photocurrent density was limited, suggesting that the overly thick coating has yielded a detrimental effect for efficient charge transfer and recombination reactions.

We extend the investigation on the photo-activities towards the influence of external bias and irradiation wavelengths with the 300 ALD cycles MoS_2 coated nanocarbon electrode, as a model for all MoS_2 coatings. Utilizing the irradiation of 660 nm, we evaluate the photo-response of the MoS_2 coated nanocarbon electrode by varying the applied potentials. Fig. 4B shows a notable change in photocurrent densities with 0.63 V_{RHE}, as a threshold potential to drive the reaction. The progressive increase in the potential to 0.83 and 1.03 V_{RHE} further increase the photocurrent densities. The most prominent increment is observed at 1.23 V_{RHE}, achieving a photocurrent density ≈0.4 mA cm^{-2}, about eight-fold than that of 0.63 V_{RHE}. Based on these results, it is apparent that the applied potential effectively assists the separation of photogenerated electron-hole pairs upon irradiation and the subsequent charge transfer process. [64]

Fig. 4C presents the photocurrent densities of the MoS_2 coated nanocarbon electrode by irradiating individual light source of different wavelengths, from the blue to the red wavelength region covering the entire visible spectral region with a constant potential of 1.23 V_{RHE}. The MoS_2 coated nanocarbon electrode has recorded a considerable response towards the irradiation of 460 nm, showing a photocurrent density of ≈0.2 mA cm^{-2}. For the irradiation of 523 and 660 nm, both the photocurrent densities were increased to ≈0.3-0.4 mA cm^{-2}, reaching twice the photocurrent density attained by the irradiation of 460 nm. The response and recovery were gradually improved by the irradiation of longer wavelength sources, i.e. shorter time was required to increase or decrease to the plateau region. For reference, the blank nanocarbon electrode was evaluated by the irradiation of 460 nm and has presented a low and unsaturated photocurrent density. The minor photoresponse is ascribed to the presence of aforementioned metal oxides impurities.[48] Nevertheless, the response from the blank electrode has an insignificant influence on the total photo-activities of the MoS_2 coated nanocarbon electrode. Inspecting the magnitude of photocurrent densities, as well as the response and recovery time, the MoS_2 coated nanocarbon electrodes favor the longer wavelength regions, which is closely connected to its optical bandgap smaller than 2.0 eV.[32–34] Despite the minor differences across different regions, consolidating the total responses, the MoS_2 is considered as photo-active in the entire visible spectral region because of the inter-d-band transitions, in line with the literature. [32–34]

On the basis of these findings, we proceed to investigate the ALD MoS_2 coated 3D nanocarbon electrodes as a photo-assisted

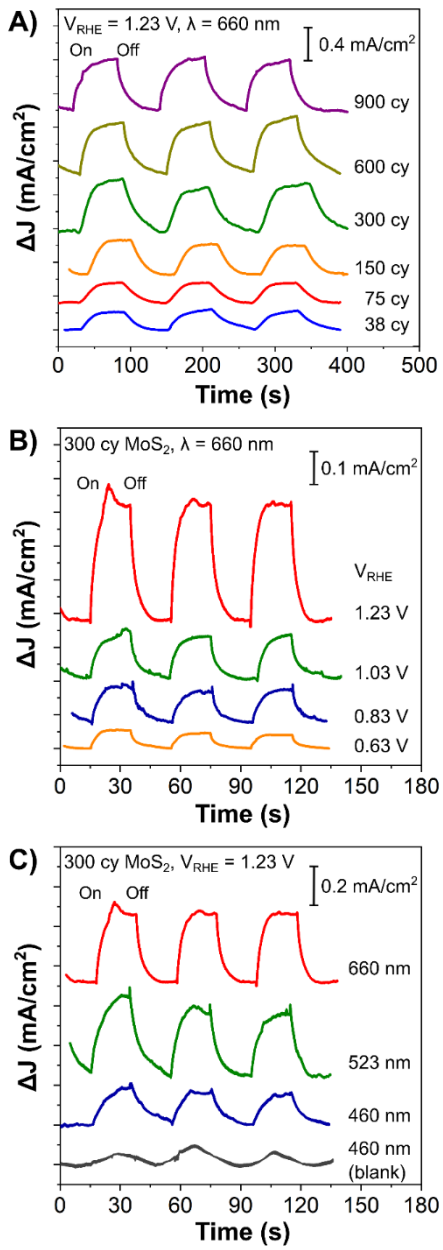

Fig. 4 Photo-responses with continuous light on/off of ALD MoS_2 coated 3D-printed nanocarbon electrode measured at different conditions: (A) 38 to 900 ALD cycles MoS_2 coated 3D-printed nanocarbon electrodes with applied potential 1.23 V_{RHE} with the irradiation source λ = 660 nm. 300 ALD cycles MoS_2 coated 3D-printed nanocarbon electrodes by (B) different applied potentials 0.63-1.23 V_{RHE} with the irradiation source λ= 660 nm, and (C) different irradiation sources, λ = 460, 523, and 660 nm with applied potential 1.23 V_{RHE}, including the blank nanocarbon electrode as reference. All measurements were carried out in 10 mM $K_3[Fe(CN)_6]$ with 0.1 M KCl electrolyte. Light on/off are marked on the first response curve for each sub-figure.

electrocatalyst for hydrogen evolution reaction (HER) with the irradiation of 660 nm. Fig. 5A,B demonstrate the linear sweep voltammetry (LSV) curves for blank and MoS_2 coated 3D nanocarbon electrodes (from 38 to 900 ALD cycles) without and with irradiation, respectively. To measure the catalytic HER performance, we compare the overpotentials by employing the standard comparison point of HER performance at -10 mA cm^{-2}. Under normal conditions (non-irradiation, dashed lines in Fig. 5A), the MoS_2 coatings have shown an overall improved catalytic HER performance by lowering the overpotential of blank nanocarbon electrode of 865 mV. Similar to many carbon-based electrodes, the blank nanocarbon electrode is arguably catalytically inactive as compared to MoS_2, thus serves as a conducting platform for the deposited material. The progressive increment to 38, 75, and 150 ALD cycles has substantially decreased the overpotential of blank nanocarbon from 865 mV to values between 470 and 490 mV. Subsequent increment to 300, 600, and 900 ALD cycles has observed a reverse behavior, despite having lower overpotential than the blank nanocarbon electrode, the values gradually increased from 652 to 751 mV. The observation is supported by the charge transfer behavior evaluated by electrochemical impedance spectroscopy (EIS) measurement. The semicircle of the Nyquist plots in Figure S4 of the ESI† was utilized to estimate the charge transfer resistance (R_{CT}). In sequence from 38 to 900 ALD cycles, the R_{CT} is 82, 62, 60, 137, 169 and 218 Ω, respectively, corroborate with the trend of HER overpotential. Upon irradiation by 660 nm (solid lines in Fig. 5B), the blank nanocarbon electrode demonstrated a rather similar overpotential, affirming their negligible photo-activity in Fig. 5A. As expected, MoS_2 coated nanocarbon electrodes have exhibited a shift to lower overpotentials according to the trend of the HER under normal condition. The lowest overpotentials were attained by MoS_2 coatings within 38 to 150 ALD cycles, in close proximity fluctuating around ≈450 mV. Similar to the normal condition, the increment to 300 to 900 ALD cycles of MoS_2 has resulted in overpotentials between 556 to 686 mV. The histogram in Fig. 5C numerically summarizes the HER overpotentials of both conditions for all MoS_2 ALD cycles for a clear overview.

The HER mechanism of MoS_2 generally follows the two main steps comprised of the initial hydronium ions (H_3O^+) adsorption and final desorption of H_2 at the surface of MoS_2.[65] Briefly, in an acidic media, hydronium ions (H_3O^+) were reduced to H_2 by consuming electrons. Meanwhile, adsorption of protons occurred on the active sites of MoS_2 to evolve H_2 via the transfer of protons and electrons or the combination of two adsorbed protons.[65,66] The described reactions took place when sufficient energy (external potential) was supplied to drive the reactions, as observed by the polarization curves in Fig. 5A. In parallel, upon irradiation of MoS_2, the incident photons were absorbed to generate electron-hole pairs. The holes are transported to the carbon electrode and then to the external circuit. Simultaneously, the electrons are excited to the MoS_2 conduction band, along with the electrons supplied by the system, reduce the protons to H_2 according to the HER mechanism described above.[67] Thereby, the additional electrons (converted from photons) facilitated the reaction with improved efficiencies by lowering the required overpotentials between 4 and 15 %, as recorded in Fig. 5C, demonstrating a photoelectrocatalytic HER effect.

The decreased HER performance of thicker MoS_2 coatings (≥ 300 cycles) is ascribed to the effect of stacking of MoS_2 nanoclusters and overlapping among them and thus reduced the exposure of active sites that are located at the edges. The

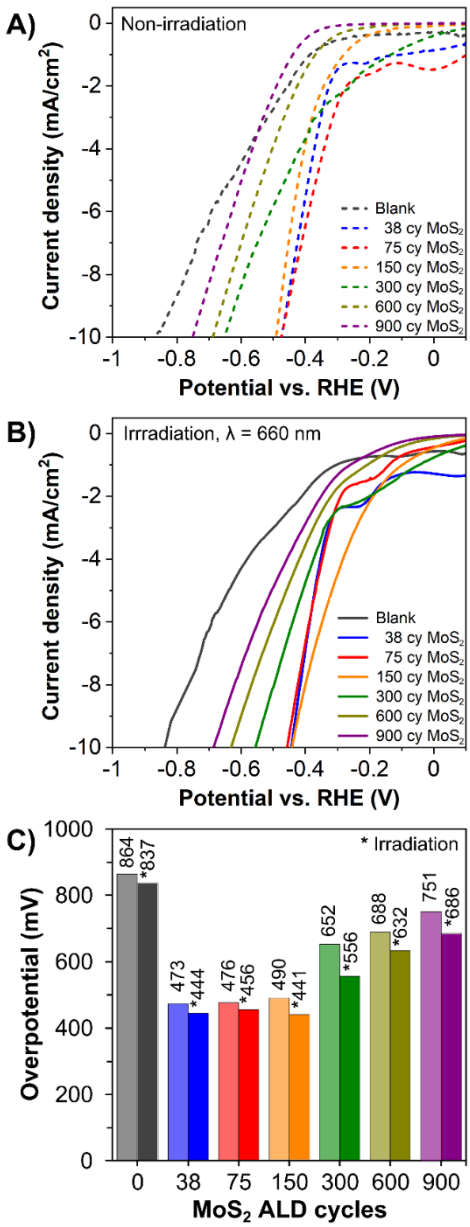

Fig. 5 Photoelectrocatalytic hydrogen evolution reaction (HER): Linear sweep voltammograms (LSV) (A) without and (B) with photo-irradiation, λ = 660 nm of blank and 38 to 900 ALD cycles MoS2 coated 3D-printed nanocarbon electrodes. LSV of the HER conditions: 0.5 M H_2SO_4 with scan rate 2 mV s^{-1}. (C) Comparison of all HER overpotentials at -10 mA cm^{-2}.

catalytic activity of MoS_2 is highly dependent on the active edges due to their faster charge transfer kinetics than that of the basal planes.[31,62,68] Based on the observation from Fig. 3 that the smaller clusters coalesced to form larger clusters, it is deduced that the stacking effect is more pronounced with thicker coatings. The lower HER activity at 600 and 900 cycles further validate that the overly thick MoS_2 with less accessible active edges is behaving more towards a bulk material. Interestingly, a more prominent photo-assisted effect was observed on the thicker coatings, well align with the results in Fig. 4A, with a general trend of higher photo-response attained by the thicker MoS_2 coatings. Despite having fewer active sites for the adsorption of protons for regular catalytic activity, the increased amount of photoactive coatings has contributed the photogenerated electrons to promote the HER activity.

A closer examination on Fig. 5A,B reveals that all electrodes have exhibited relatively sluggish kinetics, which stemmed from the base electrodes as observed in previous works.[22,23] At the initial potential sweep region, a prewave effect is observed for lower coating cycles MoS_2 and the prewave is progressively flattened by the increased amount of MoS_2 coatings. Such feature is reportedly caused by the active species of MoS_2 in HER, where the reduction of S_2^{2-} to S^{2-} occurred and accelerated the onset of HER.[37,40] Upon irradiation, all MoS_2 coated nanocarbon electrodes have shown a slightly lowered onset potential, which suggests that the irradiation efficiently initiated the reaction at an earlier point.

Overall, in Fig. 5C, the lowest overpotential ≈480 mV recorded in this work is comparable with other MoS_2 coated on 3D-printed carbon-based electrodes between ≈390 and ≈550 mV at -10 mA cm^{-2}.[22,24] We include Table S1 of the ESI† to compare the MoS_2 coated by different deposition techniques on 3D-printed electrodes. The deviations can be associated with a variety of factors including different deposition approaches, resultant stoichiometry – Mo-rich or S-rich, crystalline structure, exposed active sites – basal or edge planes, different 3D electrodes as the supporting platform and the combination of the mentioned factors.[38–40,52,54,62,68]

For reference, Tafel analyses of the polarization curves are given in Fig. S5 and the Tafel slopes are tabulated in Table S2 of the ESI. The general trend of the Tafel slope is similar to that of the trend of overpotential in Fig. 5. Briefly, the increase of MoS_2 coating up to 150 cycles decrease the Tafel slope and when the coating further increases, a reverse trend is recorded. The stability of the 300 ALD cycles MoS_2 coated 3D-printed nanocarbon electrodes is verified by applying -0.45 V (selected based on Fig. 5) to the electrode in an acidic medium for eight hours. The chronoamperometry profile recorded in Fig. S6 of the ESI† shows a consistent current density and only a minor change toward the end of the measurement.

Conclusions

We demonstrated the coating of archetypal transition metal dichalcogenide MoS_2 via atomic layer deposition (ALD) on 3D-printed nanocarbon surfaces for photo-assisted electrocatalytic hydrogen evolution reaction. The coating of MoS_2 was varied between 38 and 900 ALD cycles by the low deposition temperature, which resulted in sulfur-deficient, crystalline MoS_2 nanoclusters. The lower coating cycles with more exposed active sites have resulted in higher electrocatalytic activities, achieving an overpotential of ≈480 mV. Meanwhile, the higher coating cycles with more photo-active materials have contributed to considerable photo-enhancement in catalytic activities, yielding an overpotential of ≈450 mV. The MoS_2 coated nanocarbon electrode has demonstrated photo-response across the entire visible spectral region and higher photocurrent densities by the increased of external potential.

Our findings suggest that merging ALD and 3D-printed techniques allows limitless possibilities to design a functional device with tunable characteristics, including the material properties of a functional layer, as well as the dimensions and design of the 3D supporting platform.

Author Contributions

MP and JMM conceived the idea and designed the work. SN prepared the electrodes, measured SEM, EDX, XRD and catalytic activities. ALD process was optimized by RZ based on XPS analyses by JRP. JM carried out the HR-TEM, STEM-EDX-EELS measurement and analyses. JMM supervised ALD part of the work. MP supervised the work. All authors contributed to the writing of the manuscript.

Conflicts of interest

There are no conflicts to declare.

Acknowledgements

M.P. is supported by Grant Agency of the Czech Republic (GACR EXPRO: 19-26896X). J.M.M. thanks the Ministry of Youth, Education and Sports of the Czech Republic (MEYS CR, project LM2018103) are acknowledged for financial support of this work. S.N. and J.M. thank CEITEC Nano Research Infrastructure (MEYS CR, CzechNanoLab project LM2018110) for the use of SEM, EDX, HR-TEM, STEM-EDX-EELS, XRD and Raman spectroscopy. We thank Mr. J. Přikryl for technical ALD support, Mr. L. Hromadko for SEM measurement for initial ALD runs, and Dr. K. Ghosh for Raman spectroscopy measurement.

References

1 X. Tian, J. Jin, S. Yuan, C. K. Chua, S. B. Tor and K. Zhou, *Adv. Energy Mater.*, 2017, **7**, 1700127.
2 T. Mukherjee and T. DebRoy, *Appl. Mater. Today*, 2019, **14**, 59–65.
3 Z. Chen, Z. Li, J. Li, C. Liu, C. Lao, Y. Fu, C. Liu, Y. Li, P. Wang and Y. He, *J. Eur. Ceram. Soc.*, 2019, **39**, 661–687.
4 S. Chang, X. Huang, C. Y. Aaron Ong, L. Zhao, L. Li, X. Wang and J. Ding, *J. Mater. Chem. A*, 2019, **7**, 18338–18347.
5 K. Shen, J. Ding and S. Yang, *Adv. Energy Mater.*, 2018, **8**, 1800408.
6 Y. Li, J. Henzie, T. Park, J. Wang, C. Young, H. Xie, J. W. Yi, J. Li, M. Kim, J. Kim, Y. Yamauchi and J. Na, *Bull. Chem. Soc. Jpn.*, 2020, **93**, 176–181.
7 K. Ghosh and M. Pumera, *Nanoscale*, 2021, **13**, 5744–5756.
8 K. Sun, T.-S. Wei, B. Y. Ahn, J. Y. Seo, S. J. Dillon and J. A. Lewis, *Adv. Mater.*, 2013, **25**, 4539–4543.
9 Y. Wang, C. Chen, H. Xie, T. Gao, Y. Yao, G. Pastel, X. Han, Y. Li, J. Zhao, K. K. Fu and L. Hu, *Adv. Funct. Mater.*, 2017, **27**, 1703140.
10 A. Ambrosi, J. G. S. Moo and M. Pumera, *Adv. Funct. Mater.*, 2016, **26**, 698–703.
11 A. Ambrosi and M. Pumera, *Adv. Funct. Mater.*, 2018, **28**, 1700655.
12 C. W. Foster, M. P. Down, Y. Zhang, X. Ji, S. J. Rowley-Neale, G. C. Smith, P. J. Kelly and C. E. Banks, *Sci. Rep.*, 2017, **7**, 1–11.
13 R. M. Cardoso, D. P. Rocha, R. G. Rocha, J. S. Stefano, R. A. B. Silva, E. M. Richter and R. A. A. Muñoz, *Anal. Chim. Acta*, 2020, **1132**, 10–19.
14 F. Novotný, V. Urbanová, J. Plutnar and M. Pumera, *ACS Appl. Mater. Interfaces*, 2019, **11**, 35371–35375.
15 E. Redondo, S. Ng, J. Muñoz and M. Pumera, *Nanoscale*, 2020, **12**, 19673–19680.
16 D. M. Wirth, M. J. Sheaff, J. V. Waldman, M. P. Symcox, H. D. Whitehead, J. D. Sharp, J. R. Doerfler, A. A. Lamar and G. LeBlanc, *Anal. Chem.*, 2019, **91**, 5553–5557.
17 E. Vaněčková, M. Bouša, Š. Nováková Lachmanová, J. Rathouský, M. Gál, T. Sebechlebská and V. Kolivoška, *J. Electroanal. Chem.*, 2020, **857**, 113745.
18 C. Y. Foo, H. N. Lim, M. A. Mahdi, M. H. Wahid and N. M. Huang, *Sci. Rep.*, 2018, **8**, 7399.
19 W. Gao and M. Pumera, *Adv. Funct. Mater.*, 2021, **31**, 2007285.
20 K.-E. E. Guima, V. H. R. R. Souza and C. A. Martins, *RSC Adv.*, 2019, **9**, 15158–15161.
21 E. Redondo and M. Pumera, *Electrochem. Commun.*, 2021, **124**, 106920.
22 R. Gusmão, Z. Sofer, P. Marvan and M. Pumera, *Nanoscale*, 2019, **11**, 9888–9895.
23 S. Ng, C. Iffelsberger, Z. Sofer and M. Pumera, *Adv. Funct. Mater.*, 2020, **30**, 1910193.
24 C. Iffelsberger, S. Ng and M. Pumera, *Appl. Mater. Today*, 2020, **20**, 100654.
25 K. A. Novčić, C. Iffelsberger, S. Ng and M. Pumera, *Nanoscale*, 2021, **13**, 5324–5332.
26 D. Voiry, J. Yang and M. Chhowalla, *Adv. Mater.*, 2016, **28**, 6197–6206.
27 A. Eftekhari, *Int. J. Hydrogen Energy*, 2017, **42**, 11053–11077.
28 Z. Li, X. Meng and Z. Zhang, *J. Photochem. Photobiol. C Photochem. Rev.*, 2018, **35**, 39–55.
29 M. Motola, M. Baudys, R. Zazpe, M. Krbal, J. Michalička, J. Rodriguez-Pereira, D. Pavliňák, J. Přikryl, L. Hromádko, H. Sopha, J. Krýsa and J. M. Macak, *Nanoscale*, 2019, **11**, 23126–23131.
30 B. Hinnemann, P. G. Moses, J. Bonde, K. P. Jørgensen, J. H. Nielsen, S. Horch, I. Chorkendorff and J. K. Nørskov, *J. Am. Chem. Soc.*, 2005, **127**, 5308–5309.
31 A. B. Laursen, S. Kegnæs, S. Dahl and I. Chorkendorff, *Energy Environ. Sci.*, 2012, **5**, 5577–5591.
32 G. L. Frey, R. Tenne, M. J. Matthews, M. S. Dresselhaus and G. Dresselhaus, *J. Mater. Res.*, 1998, **13**, 2412–2417.
33 K. K. Kam and B. A. Parkinson, *J. Phys. Chem.*, 1982, **86**, 463–467.
34 J. A. Wilson and A. D. Yoffe, *Adv. Phys.*, 1969, **18**, 193–335.
35 M. Velický and P. S. Toth, *Appl. Mater. Today*, 2017, **8**, 68–103.
36 Y. Huang and L. Liu, *Sci. China Mater.*, 2019, **62**, 913–924.
37 X. Chia, N. A. A. Sutrisnoh and M. Pumera, *ACS Appl. Mater. Interfaces*, 2018, **10**, 8702–8711.
38 F. Xi, P. Bogdanoff, K. Harbauer, P. Plate, C. Höhn, J. Rappich, B. Wang, X. Han, R. Van De Krol and S. Fiechter, *ACS Catal.*, 2019,

9, 2368–2380.
39 S. Oh, J. B. Kim, J. T. Song, J. Oh and S.-H. Kim, *J. Mater. Chem. A*, 2017, **5**, 3304–3310.
40 D. Merki, S. Fierro, H. Vrubel and X. Hu, *Chem. Sci.*, 2011, **2**, 1262–1267.
41 M. Ritala and J. Niinisto, in *Chemical Vapour Deposition: Precursors, Processes and Applications*, eds. A. C. Jones and M. L. Hitchman, Royal Society of Chemistry, 2009, pp. 158–206.
42 S. E. Potts, H. B. Profijt, R. Roelofs and W. M. M. M. Kessels, *Chem. Vap. Depos.*, 2013, **19**, 125–133.
43 H. Sopha, A. T. Tesfaye, R. Zazpe, J. Michalicka, F. Dvorak, L. Hromadko, M. Krbal, J. Prikryl, T. Djenizian and J. M. Macak, *FlatChem*, 2019, **17**, 100130.
44 M. Leskelä, M. Mattinen and M. Ritala, *J. Vac. Sci. Technol. B*, 2019, **37**, 030801.
45 S. Ng, C. Iffelsberger, J. Michalička and M. Pumera, *ACS Nano*, 2021, **15**, 686–697.
46 M. P. Browne, J. Plutnar, A. M. Pourrahimi, Z. Sofer and M. Pumera, *Adv. Energy Mater.*, 2019, **9**, 1900994.
47 R. van de Krol and M. Graetzel, *Photoelectrochemical Hydrogen Production*, Springer US, Boston, MA, 2012, vol. 102.
48 M. P. Browne, V. Urbanova, J. Plutnar, F. Novotný and M. Pumera, *J. Mater. Chem. A*, 2020, **8**, 1120–1126.
49 H. W. Wang, P. Skeldon and G. E. Thompson, *Surf. Coatings Technol.*, 1997, **91**, 200–207.
50 P. A. Spevack and N. S. McIntyre, *J. Phys. Chem.*, 1992, **96**, 9029–9035.
51 T. Weber, J. C. Muijsers and J. W. Niemantsverdriet, *J. Phys. Chem.*, 1995, **99**, 9194–9200.
52 H. Vrubel, D. Merki and X. Hu, *Energy Environ. Sci.*, 2012, **5**, 6136–6144.
53 M. Mattinen, T. Hatanpää, T. Sarnet, K. Mizohata, K. Meinander, P. J. King, L. Khriachtchev, J. Räisänen, M. Ritala and M. Leskelä, *Adv. Mater. Interfaces*, 2017, **4**, 1700123.
54 T.-W. Lin, C.-J. Liu and J.-Y. Lin, *Appl. Catal. B Environ.*, 2013, **134**–**135**, 75–82.
55 S. Ng, M. Krbal, R. Zazpe, J. Prikryl, J. Charvot, F. Dvořák, L. Strizik, S. Slang, H. Sopha, Y. Kosto, V. Matolin, F. K. Yam, F. Bures and J. M. Macak, *Adv. Mater. Interfaces*, 2018, **5**, 1701146.
56 R. Zazpe, J. Charvot, R. Krumpolec, L. Hromádko, D. Pavliňák, F. Dvorak, P. Knotek, J. Michalicka, J. Přikryl, S. Ng, V. Jelínková, F. Bureš and J. M. Macak, *FlatChem*, 2020, **21**, 100166.
57 J. J. Pyeon, S. H. Kim, D. S. Jeong, S.-H. Baek, C.-Y. Kang, J.-S. Kim and S. K. Kim, *Nanoscale*, 2016, **8**, 10792–10798.
58 T. Jurca, M. J. Moody, A. Henning, J. D. Emery, B. Wang, J. M. Tan, T. L. Lohr, L. J. Lauhon and T. J. Marks, *Angew. Chemie Int. Ed.*, 2017, **56**, 4991–4995.
59 E. Fitzer, K.-H. Kochling, H. P. Boehm and H. Marsh, *Pure Appl. Chem.*, 1995, **67**, 473–506.
60 V. Petkov, S. J. L. L. Billinge, P. Larson, S. D. Mahanti, T. Vogt, K. K. Rangan and M. G. Kanatzidis, *Phys. Rev. B*, 2002, **65**, 092105.
61 Y. Wu, M. H. Raza, Y.-C. Chen, P. Amsalem, S. Wahl, K. Skrodczky, X. Xu, K. S. Lokare, M. Zhukush, P. Gaval, N. Koch, E. A. Quadrelli and N. Pinna, *Chem. Mater.*, 2019, **31**, 1881–1890.
62 T. F. Jaramillo, K. P. Jorgensen, J. Bonde, J. H. Nielsen, S. Horch and I. Chorkendorff, *Science (80-.).*, 2007, **317**, 100–102.
63 C. Marichy and N. Pinna, *Coord. Chem. Rev.*, 2013, **257**, 3232–3253.
64 W. W. Gärtner, *Phys. Rev.*, 1959, **116**, 84–87.
65 T. Shinagawa, A. T. Garcia-Esparza and K. Takanabe, *Sci. Rep.*, 2015, **5**, 1–21.
66 V. Nguyen, T. P. Nguyen, T. Le, D. N. Vo, D. L. T. Nguyen, Q. T. Trinh, I. T. Kim and Q. Van Le, *J. Chem. Technol. Biotechnol.*, 2020, **95**, 2597–2607.
67 K. C. Kwon, S. Choi, K. Hong, C. W. Moon, Y. S. Shim, D. H. Kim, T. Kim, W. Sohn, J. M. Jeon, C. H. Lee, K. T. Nam, S. Han, S. Y. Kim and H. W. Jang, *Energy Environ. Sci.*, 2016, **9**, 2240–2248.
68 S. M. Tan, A. Ambrosi, Z. Sofer, Š. Huber, D. Sedmidubský and M. Pumera, *Chem. - A Eur. J.*, 2015, **21**, 7170–7178.

